OPTICA

Coherent multidimensional widefield microscopy

Mohammadjavad Azarm,[1,2,3] Rizwan Asif,[1,2,4] Alessandra Milloch,[1,2,3] Francesco Proietto,[1,2,3] Donna Datta,[5] Ambrine Lanseur,[6] Sreyan Raha,[7] Filippo Fabbri,[7] Federica Bianco,[7] Fabrizio Preda,[8] Antonio Perri,[8] Suman Chatterjee,[9] Ziliang Ye,[9,10] Giulio Cerullo,[11,12] Stefania Pagliara,[1,2] Gabriele Ferrini,[1,2] and Claudio Giannetti[1,2,13,*]

[1]Department of Mathematics and Physics, Università Cattolica del Sacro Cuore, Brescia I-25133, Italy
[2]ILAMP (Interdisciplinary Laboratories for Advanced Materials Physics), Università Cattolica del Sacro Cuore, Brescia I-25133, Italy
[3]Department of Physics and Astronomy, KU Leuven, B-3001 Leuven, Belgium
[4]Department of Biosystems, KU Leuven, B-3001 Leuven, Belgium
[5]Elmore Family School of Electrical and Computer Engineering, Purdue University, 465 Northwestern Ave, West Lafayette, Indiana 47907, USA
[6]Université Claude Bernard Lyon 1, Villeurbanne, France
[7]NEST Laboratory, Istituto Nanoscienze-CNR, Piazza S. Silvestro 12, I-56127 Pisa, Italy
[8]NIREOS SRL, Via G. Durando 39, 20158 Milano, Italy
[9]Quantum Matter Institute, University of British Columbia, Vancouver, British Columbia V6T 1Z4, Canada
[10]Department of Physics & Astronomy, University of British Columbia, Vancouver, British Columbia V6T 1Z1, Canada
[11]Department of Physics, Politecnico di Milano, Piazza Leonardo da Vinci 32, I-20133 Milano, Italy
[12]IFN-CNR, Piazza Leonardo da Vinci 32, I-20133 Milano, Italy
[13]CNR-INO (National Institute of Optics), via Branze 45, 25123 Brescia, Italy
*claudio.giannetti@unicatt.it

Received 20 January 2026; revised 16 June 2026; accepted 6 July 2026; published 8 September 2026

Understanding how electronic excitations evolve across space and time is essential for revealing the microscopic processes underlying quantum and optoelectronic materials. However, existing approaches cannot simultaneously resolve ultrafast coherent dynamics with microscopic spatial information: pump–probe microscopy lacks access to quantum coherence, while two-dimensional electronic spectroscopy (2DES) requires slow point-by-point scanning for spatial resolution. Here, we introduce a widefield two-dimensional electronic spectroscopy microscope (2DESM) combining multidimensional coherent spectroscopy with widefield imaging, enabling simultaneous femtosecond temporal and micrometer spatial resolution across a broadband spectral range. Applying 2DESM to hBN-encapsulated WSe_2, we directly visualize spatial variations in exciton coherence and relaxation associated with the local environment, establishing 2DESM as a powerful platform for probing many-body interactions, energy transport, and structure–function relationships in low-dimensional materials and devices. © 2026 Optica Publishing Group under the terms of the Optica Open Access Publishing Agreement

https://doi.org/10.1364/OPTICA.590834

1. INTRODUCTION

Recent advances in the synthesis of low-dimensional quantum materials [1,2], van der Waals heterostructures [3,4], and nanodot artificial solids [5–8] have underscored the need for advanced spectroscopic techniques capable of studying fundamental ultrafast electronic processes with both spectral and spatial resolution [9]. Transition metal dichalcogenides (TMDs) [10,11] represent a paradigmatic system, in which well-defined optical excitons can experience spatially dependent interlayer and intralayer potentials in heterostructures [12–16] and moiré potentials in twisted bilayers [17–19]. Under strong excitation, TMDs are test bed for spatially inhomogeneous excitonic Mott transitions [20,21] as well as for the formation of many-body complexes such as biexcitons and trions [22]. Furthermore, the reduced dimensionality and structural heterogeneity [19] boost microscale phenomena including exciton diffusion [19,23], charge transfer [24,25], and edge-localization [26]. So far, conventional approaches to studying non-equilibrium dynamics in these systems have predominantly relied on ultrafast pump–probe spectro-microscopy [27–29], which consists of the combination of broadband pump–probe optical spectroscopy with microscopy. This approach is effective in probing the space-dependent population dynamics [30–34], but it is inherently insensitive to those processes that involve the quantum-coherent evolution of the macroscopic polarization. Examples are the ultrafast quantum coherent evolution of the electronic wave-packets [35], the inhomogeneous broadening associated with local disorder [36], and the coherent coupling between different electronic states [37], which impact both the fundamental understanding and the device performance. Multidimensional electronic spectroscopy [38,39], based on the excitation with multiple phase-coherent light pulses, has emerged

as the go-to technique to overcome many of the intrinsic limitations of traditional pump–probe techniques. In the case of two phase-coherent excitation pulses, two-dimensional electronic spectroscopy (2DES) allows to correlate excitation and detection frequencies while simultaneously preserving high spectral and temporal resolution, thereby allowing the direct observation of coherent dynamics, energy-transfer pathways, and many-body interactions with femtosecond precision [1,40–45]. 2DES has proven especially powerful in disentangling homogeneous and inhomogeneous broadening [36,46], providing access to the intrinsic linewidth of optical excitations even in spectrally disordered systems [1]. It also enables the identification of electronic couplings, energy-transfer pathways, and coherent interactions between states [38].

Efforts to complement multidimensional spectroscopies with spatial resolution have so far primarily relied on point-scanning approaches employing tightly focusing optics [47–50] or on tip-enhanced nanoimaging [51]. Here, we present a widefield microscope integrating the capabilities of conventional 2DES, which we refer to as 2DESM. This setup preserves high temporal resolution (tens of femtoseconds) and broad spectral bandwidth, and enables time-resolved spectral imaging that captures ultrafast coherent electronic dynamics with micrometer-scale resolution. We apply 2DESM to investigate the ultrafast coherent excitonic dynamics in a bilayer WSe_2 flake encapsulated by hBN, which provides a clean, strain-minimized environment preserving the intrinsic optical properties of the material. We demonstrate the possibility of measuring space-dependent 2DES maps and extracting direct information about the local decoherence dynamics and the disorder-induced broadening of excitonic lines in WSe_2. More generally, this novel integrated platform paves the way for studying quantum-coherent wave-packet propagation, space diffusion of excitons and many-body complexes (e.g., biexcitons and trions), and non-local coherent energy exchange between different electronic excitations, with broad application to low-dimensional materials, van der Waals heterostructures [52], and micrometer-sized optoelectronic devices.

2. 2DES MICROSCOPY

Our technique builds on 2DES, a non-linear optical spectroscopy grounded in four-wave mixing (FWM) [38,53]. In this scheme, a third-order polarization $P^{(3)}(t)$ is generated through the interaction of three ultrafast laser pulses, i.e., two phase-coherent pump pulses and a third delayed probe, with the sample. By simultaneously resolving excitation and detection frequencies, 2DES extends the capabilities of conventional one-dimensional time-resolved techniques, such as broadband pump–probe spectroscopy, generating two-dimensional correlation maps that reveal couplings and dynamics inaccessible to standard approaches [29].

The standard 2DES signal is given by

$$S(\omega_{pu}, \omega_{pr}, t_{del}), \tag{1}$$

where ω_{pu} denotes the excitation (pump) frequency, ω_{pr} the detection (probe) frequency, and t_{del} the time delay between the pump and probe pulses. To measure $S(\omega_{pu}, \omega_{pr}, t_{del})$, a pair of phase-locked pump pulses spaced by a controllable time delay t_{pu} is used to create a coherent superposition of quantum states. Scanning t_{pu} and performing a Fourier transform (FT) yield the excitation frequency axis ω_{pu} of the 2D spectrum. After interacting with the two pump pulses, the system is probed by the third pulse. The emitted signal is spectrally resolved by an interferometric spectrometer, providing resolution along the detection frequency axis (ω_{pr}). We note that, although in conventional 2DES notation the coherence and waiting times are denoted by t_1 and t_2, respectively [54], in this work, they will be indicated as t_{pu} and t_{del} for the sake of simplicity in describing the experimental setup and the data-acquisition procedure. The implementation of 2DES in a partially collinear geometry [55,56] simplifies phase matching, enhances alignment stability, and supports transmission-based detection—features that make it particularly well-suited for studying complex condensed matter systems [38,43,57].

Here, we extend 2DES into the spatial domain by collecting the probe pulse, after the interaction of the pulses with the sample, via an optical widefield microscope. In this way, it is possible to perform optical imaging of the sample with high spatial resolution, without losing the temporal and multidimensional spectral information. Each set of acquired data corresponds to a specific pair of excitation and detection frequencies, (ω_{pu}, ω_{pr}), that evolve as a function of the time delay t_{del} [Eq. (1)], while spatial coordinates (x, y) define the position within the field of view. The full data volume is then expressed as

$$S(x, y; \omega_{pu}, \omega_{pr}; t_{del}) \tag{2}$$

and contains spatially resolved 2DES maps.

A. Optical Setup

In Fig. 1(a), we show a sketch of the 2DESM setup. The light source is a home-built non-collinear optical parametric amplifier (NOPA), pumped by an amplified Yb:KGW laser (Pharos by Light Conversion) delivering 37.5 μJ pulses at a 400 kHz repetition rate. The NOPA generates broadband pulses, tunable from 1.4 to 2.1 eV. Figure 1(b) shows the typical NOPA spectrum, centered at 1.70 eV and covering the 1.41–1.82 eV spectral range. The NOPA output beam is split to feed both the pump and probe lines. The pump arm passes through an interferometric collinear pulse generator (ICPG) (GEMINI 2D by NIREOS). The ICPG is based on the Translating-Wedge-based Identical Pulses eNcoding System (TWINS) scheme, as introduced in Ref. [58], in which birefringent elements introduce a precisely controlled optical delay between two temporally separated replicas of the pulse traveling along a common optical path. The ICPG generates two pulses at a variable time delay t_{pu}, with phase stability of the order of 1/1000 of the optical cycle. The pump–probe time delay t_{del} is controlled by the mechanical delay stage, which introduces an additional delay by adjusting the pump path with respect to the probe optical path. Due to the pulse stretching caused by propagation through optical components, such as polarizers, waveplates, and crystals inside the ICPG, two distinct pulse compressors based on pairs of chirped mirrors are employed for the pump and probe beams, respectively. Subsequently, the beams are focused onto the sample using concave mirrors with focal lengths of 40 cm for the pump and 20 cm for the probe, resulting in spot diameters (FWHM) of ∼190 and ∼100 μm for the pump and probe beams, respectively. To collect the probe beam after its interaction with the sample excited by the pump pulses, we use a wide-field objective with 20× magnification, a 20 mm working distance, and a 0.40 numerical aperture. An infinity-corrected tube lens with a 200 mm focal length and a 151.8 mm working distance, operating in the 1.2–1.9 eV spectral

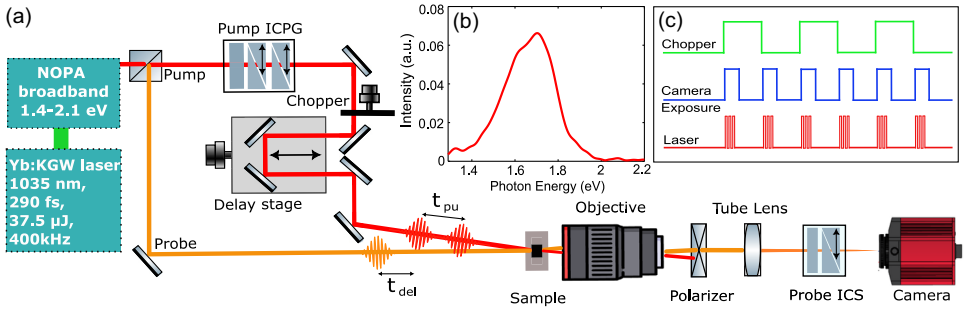


Fig. 1. (a) Schematic of the 2DESM setup. The light source is a home-built non-collinear optical parametric amplifier (NOPA). The NOPA produces broadband light tunable from 1.4 to 2.1 eV, generating spectrally identical pump and probe pulses. A pair of pump pulses is generated by the interferometric collinear pulse generator (ICPG), which creates two phase-locked replicas with a controllable time delay t_{pu}. The pump–probe delay t_{del} is introduced via a mechanical delay stage, and the chopper provides the timing reference for synchronizing acquisition. After interaction with the sample, a wide-field objective and tube lens image the transmitted probe onto the camera, while a polarizer suppresses residual pump scattering to enhance the SNR. The interferometric collinear spectrometer (ICS) is placed after the tube lens and generates two temporally delayed probe pulses with delay t_{pr}. The black double arrow in both the ICPG and ICS indicates the wedge translation direction. (b) NOPA spectrum. The NOPA output is centered at 1.70 eV, covering a range from 1.41 to 1.82 eV. (c) Timing diagram of the triggering system. The chopper serves as the master timing reference, while the camera acquires two frames per chopper duty cycle. Each camera acquisition triggers the laser to emit a defined number of pulses, set by the camera exposure time. In this scheme, the chopper blocks the pump beam for one of the two frames, yielding one frame with the pump on and one with the pump blocked.

range, images the sample onto the camera used for detection. A scientific high-speed camera (CS135MUN by Thorlabs) is used for rapid data acquisition synchronized with the laser source emission. The camera features a 1280 × 1024 pixel detector array (∼1.3MP), with a pixel dimension of 4.8 × 4.8 µm^2. By selectively cropping regions from the full frame, we are able to increase the imaging speed up to 3469 frames per second with a minimum exposure time of 0.1 ms.

To extend 2DESM measurements to cryogenic temperatures, a custom cryogenic chamber was designed and integrated into a closed-cycle cryostat system. The chamber is equipped with a 1.5 mm thick optical entrance window; the residual dispersion introduced by this element is pre-compensated by the chirped-mirror compressors. A 200 µm thick optical exit window, placed between the sample and the microscope objective, allows the objective to operate at its nominal working distance, preserving both the numerical aperture and the spatial resolution of the imaging system while minimizing optical aberrations. Low-temperature operation of the 2DESM platform is demonstrated in Section 4, where measurements on WSe_2 at 20 K are presented.

B. Hyperspectral Data Acquisition

The synchronization between image acquisition and light pulses is essential to improve the signal-to-noise ratio (SNR) and extract the weak difference between pumped and unpumped images, as shown in the timing diagram of Fig. 1(c). A chopper wheel, positioned on the pump path, serves as the master timing reference (clock), triggering the camera to acquire two frames per cycle, corresponding to the pump pulse on and off, respectively. The clock signal [green line in Fig. 1(c)] is used to generate synchronized digital triggers for both the laser emission and the camera acquisition, thus ensuring that a controllable number of laser pulses is emitted within the camera's exposure window. The number of laser pulses per cycle and individual delay offsets are tunable parameters, which can be adapted and optimized depending on various experimental conditions. For each chopper cycle, we acquire two distinct image streams ($I_i(x, y)$) corresponding to pumped (i: even) and unpumped (i: odd) signals. At a 1.5 kHz chopping rate, the camera records ≃ 3000 frames per second. To compensate for intensity fluctuations and enhance the SNR, each image $I_i(x, y)$ is normalized, frame by frame, to its background intensity, $\overline{I_i}$. This is achieved by selecting a sub-region far enough from the sample, where no pump-induced signal is expected, and integrating the total intensity detected by the camera within the selected region. This high-speed normalization ensures consistency across frames by accounting for frame-to-frame variations in illumination and detector response [59,60]. For each value of t_{pu} and t_{del}, we then compute the mean pumped ($\overline{T}_{pumped}$) and unpumped ($\overline{T}_{unpumped}$) transmitted intensity signals by averaging over N acquired frames as

$$\overline{T}_{pumped} = \frac{1}{N} \sum_{\substack{i=1 \\ even}}^{N} \frac{I_i(x, y; t_{pu}, t_{del})}{\overline{I_i}}, \tag{3}$$

$$\overline{T}_{unpumped} = \frac{1}{N} \sum_{\substack{i=1 \\ odd}}^{N} \frac{I_i(x, y; t_{pu}, t_{del})}{\overline{I_i}}. \tag{4}$$

The relative transmittivity variation signal for fixed t_{pu} and t_{del} is obtained as

$$\Delta T(x, y; t_{pu}, t_{del}) = \overline{T}_{pumped} - \overline{T}_{unpumped}. \tag{5}$$

Within this imaging scheme, frequency resolution along the probe axis of the 2D spectrum is obtained by means of an interferometric collinear spectrometer (ICS) (GEMINI by NIREOS), which is a simplified version of the ICPG previously introduced. Two birefringent wedges introduce a precisely controlled optical delay t_{pr} [58] between two replicas of the probe light traveling along a common optical path from the tube lens to the camera [see Fig. 1(a)] [61]. Application of the FT to the modulated patterns returns the spectral content of the probe beam while preserving spatial resolution.

Overall, the coordinated action of the ICPG on the pump beam, which controls t_{pu}, and the ICS on the probe, which controls t_{pr}, enables to perform 2DES spectroscopy combined with wide-field microscopy (2DESM). Figure 2 shows the overall acquisition

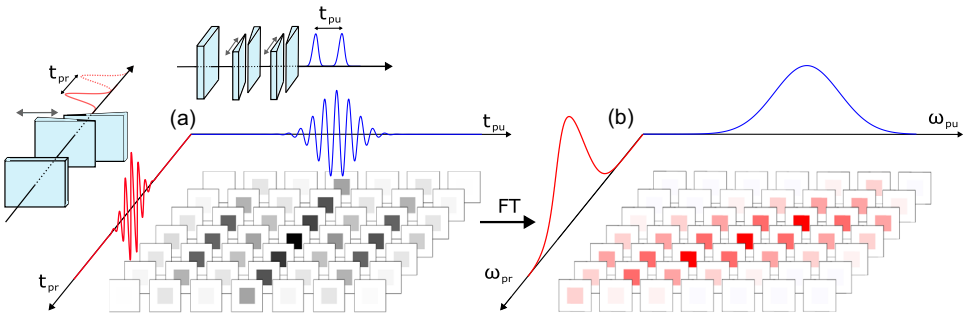


Fig. 2. (a) Time-domain hypercube. Schematics of the construction of the $S(x, y; t_{pu}, t_{pr}, t_{del})$ time-domain hypercube at the fixed pump–probe delay t_{del}. Each image, represented by the black squares, corresponds to a specific (t_{pu}, t_{pr}) coordinate. The top sketches illustrate the ICPG and ICS devices with black double arrows indicating the direction of translating wedges to control the t_{pu} and t_{pr} coordinates. The red and blue interferograms represent the typical signals obtained for fixed (x, y) spatial coordinates upon scanning the t_{pu} and t_{pr} axes. (b) Frequency-domain hypercube. A two-dimensional FT is applied to each image pixel, thus converting the time-domain $S(x, y; t_{pu}, t_{pr}, t_{del})$ hypercube into the frequency-domain hypercube $S(x, y; \omega_{pu}, \omega_{pr}, t_{del})$.

process. At a fixed pump–probe delay t_{del}, a $\Delta T(x, y; t_{pu}, t_{del})$ image [see Eq. (5)] is recorded for each step of t_{pu}. The scanning across multiple values of t_{pu} forms a data stack. A second scan is performed along the t_{pr} dimension, thus producing a multidimensional dataset (hypercube), i.e., $\Delta T(x, y; t_{pu}, t_{pr}, t_{del})$. A two-dimensional FT is then applied to extract the spectral information along both excitation and detection axes. The resulting two-dimensional signal is obtained by

$$S(x, y; \omega_{pu}, \omega_{pr}, t_{del}) = \iint \Delta T(x, y; t_{pu}, t_{pr}, t_{del}) \times e^{-i\omega_{pu}t_{pu}} e^{-i\omega_{pr}t_{pr}} \, dt_{pu} \, dt_{pr}. \quad (6)$$

Finally, to provide a calibrated and quantitative response, the spectrum at each pixel is normalized to the probe spectrum, correcting for spectral non-uniformities and referencing the signal to its equilibrium value. This procedure is repeated for each pixel of the image, corresponding to the coordinate (x, y). As shown in Fig. 2, this dual-scanning strategy yields, at a fixed t_{del}, a multidimensional hyperspectral data cube, with both excitation (ω_{pu}) and detection (ω_{pr}) spectral dimensions derived from the temporal delays controlled by the ICPG and the ICS. 2DESM thus enables the multidimensional investigation of ultrafast coherent excitation dynamics in real materials and devices with high spatial resolution. As shown in Fig. 3, at a selected pump–probe delay (t_{del}), a hyperspectral $S(x, y; \omega_{pu}, \omega_{pr}, t_{del})$ data cube is acquired. The top-right panel of Fig. 3 shows a typical 2DES map that can be extracted at a specific (x, y) point. In the sketched example, the signal, elongated along the image diagonal, represents the pump-induced variation of an excitonic resonance, whose decoherence time and inhomogeneous broadening can be extracted from the analysis of the diagonal and off-diagonal line profiles, as will be discussed extensively in Section 3.

C. 2DESM Resolution

A comprehensive assessment of the 2DESM setup performance was conducted by characterizing its temporal, spatial, and spectral resolution. Temporal resolution was evaluated using polarization-gated frequency-resolved optical gating (PG-FROG) [62]. Figure 4(a) shows the cross-correlation signal between pump and probe pulses, at the sample position, obtained by integrating the PG-FROG trace along the wavelength axis. The inset of

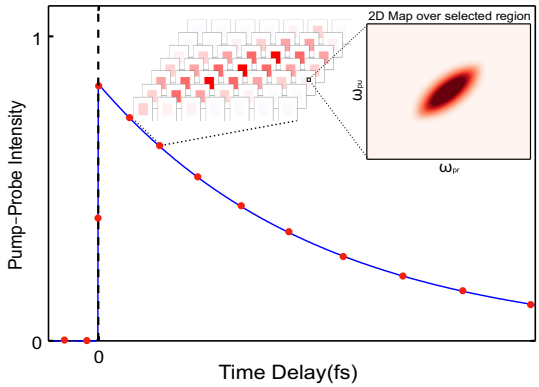


Fig. 3. Ultrafast 2DESM temporal dynamics. Illustration of the full 2DESM acquisition process. For each pump–probe delay t_{del}, a full frequency-domain hypercube $S(x, y; \omega_{pu}, \omega_{pr}, t_{del})$ is acquired. For each spatial coordinate (x, y), a time-dependent 2DES spectrum, as shown in the top-right panel, is obtained.

Fig. 4(a) shows the full PG-FROG trace, representing the cross-correlation as a function of the time delay and the wavelength. The measured full width at half-maximum (FWHM) of the cross-correlation signal is 55 fs. Assuming identical Gaussian temporal profiles for both pulses, we estimated an individual pulse duration of approximately 38 fs on the sample. This value defines the temporal resolution limit of our system, which is not altered by the optical components (objective, tube lens, and ICS) that collect the probe light after the non-linear interaction.

Spatial resolution was determined by imaging a sub-micrometer defect and analyzing its Airy disk diffraction pattern, as shown in Fig. 4(b). Considering half the distance between the first two intensity minima, the spatial resolution results to be approximately 1.05 μm. The inset of Fig. 4(b) shows the image of the point-like defect, highlighting the resulting diffraction pattern under laser illumination.

In the TWINS scheme, the spectral resolution is controlled by the maximum temporal delay introduced via the translation of birefringent wedges [63]. This resolution can be quantitatively estimated using the relation:

$$\Delta\nu = \frac{c}{\Delta n L \tan(\alpha)}, \quad (7)$$

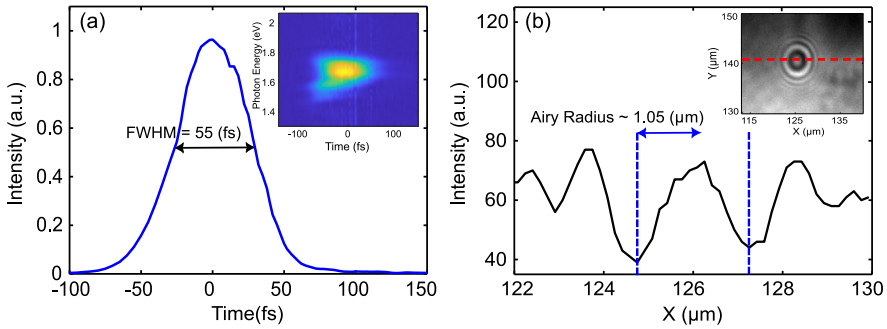


Fig. 4. (a) Pulse duration. The main panel displays the temporal profile obtained by integrating the PG-FROG signal (shown in the inset). (b) Spatial resolution. The main panel displays the line profile extracted from the diffraction pattern of a point-like defect. The spatial resolution of the system is estimated as half the distance between the first two minima of the Airy disk. The diffraction pattern from the point-like defect is shown in the top-right panel. The red dashed line indicates the line along which the intensity profile shown in the main panel is taken.

where c is the speed of light, Δn represents the difference between the refractive indices of the ordinary and extraordinary polarization components, and L is the total displacement range of the wedge with the apex angle α. Since the spectral resolution is inversely proportional to the maximum delay, increasing the displacement range L enhances the resolution. To strike a balance between spectral resolution and acquisition speed, the wedge displacement range is selected as $L = 1.2$ mm. Using birefringent wedges of the BBO material ($\Delta n = -0.1152$ at 800 nm [64]) with an apex angle of $\alpha = 10°$, the spectral resolution was determined to be $\Delta\lambda = 22$ nm at a 800 nm central wavelength, corresponding to an energy resolution of 50 meV at 1.5 eV.

3. 2DESM ON BILAYER WSe_2

TMDs constitute the ideal test bench for the 2DESM technique introduced in this work. The preparation of the monolayer or few-layer samples via mechanical exfoliation typically yields micrometer-sized flakes, necessitating microscopy-based approaches. In terms of optical properties, the bi-dimensional nature of TMDs' atomic layers strongly suppresses bulk Coulomb screening, thus giving rise to well-defined excitons with a large binding energy compared to bulk semiconductors [11]. More specifically, a band gap of 2.53 eV and a binding energy of $E_b^A = 0.79$ eV have been reported at $T = 4$ K for the A-exciton in WSe_2 monolayers deposited on SiO_2 [65]. The main excitonic line thus corresponds to a photon energy of $E_{\mathrm{exc}}^A = 1.74$ eV. Considering the typical band-edge redshift of semiconductors associated with electron-phonon coupling [66], at $T = 300$ K, the A-exciton energy decreases down to $E_{\mathrm{exc}}^A \simeq 1.65$ eV [65], which lies at the center of the pulse bandwidth [see Fig. 1(b)].

Here, we apply 2DESM to investigate a bilayer WSe_2 flake placed on a transparent glass substrate, as shown in Fig. 5(a). WSe_2 (green dashed contour) has been encapsulated by bottom (light blue dashed contour) and top (white dashed contour) layers of hBN. The sample area measures approximately 15×15 μm^2 (green dashed line) and contains two distinct regions: (1) approximately at the center of the image, WSe_2 is encapsulated by both top and bottom hBN layers. The black rectangular area is taken as representative of fully encapsulated WSe_2; (2) the top-left region of the sample is not covered by the top hBN overlayer. The red rectangular area is taken as representative of unprotected WSe_2.

To characterize the sample, photoluminescence (PL) measurements were conducted. As shown in Fig. 5(b), the PL spectrum

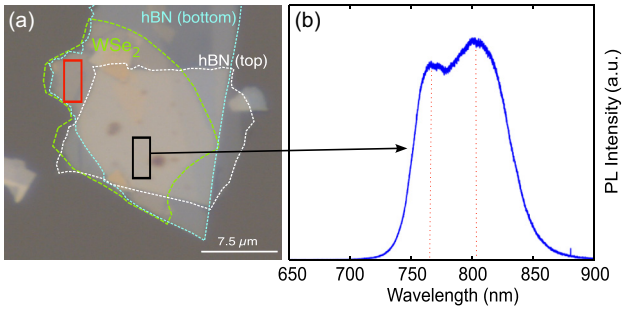


Fig. 5. (a) Bilayer WSe_2. An optical image of the sample, taken with a 50× objective, is shown. The bilayer WSe_2 flake, indicated by the green contour, was mechanically exfoliated and deposited on a SiO_2 substrate covered by a hBN layer (light blue contour). The top side of WSe_2 has been protected by an additional hBN overlayer, indicated by the white contour. The black and red rectangles indicated the two regions that are taken as representative of the fully encapsulated and unprotected WSe_2 bilayer. (b) Photoluminescence**.** Photoluminescence measurements from the black rectangular area of panel (a) are shown. The spectrum displays two distinct peaks at 770 and 810 nm (see dashed red lines), consistent with emission from the bilayer WSe_2 [67,68].

from the central area of the sample exhibits a weak emission peak near 770 nm (1.61 eV) and a second peak near 810 nm (1.53 eV), characteristic of indirect excitonic recombination in the bilayer WSe_2. The presence of this secondary peak and the reduced intensity indicates interlayer coupling effects that modify the electronic band structure, confirming the bilayer nature of the WSe_2 flake [67,68].

Figure 6 shows the results of the 2DESM measurements performed on the bilayer WSe_2 at $T = 300$ K. The excitation fluence is ≈ 30 μJ cm^{-2}, distributed over a circular spot with a ∼190 μm diameter (FWHM). The probe beam is spectrally identical to the pump and has a total pulse energy ≈ 10 times lower. The images are cropped down to a size of 140 × 120 pixels and are acquired at a frequency of 3 kHz, with an integration time of 1 s. For each camera frame, whose acquisition is triggered by the chopper status [see the scheme in Fig. 1(c)], six laser pulses are emitted. The $S(x, y; \omega_{\mathrm{pu}}, \omega_{\mathrm{pr}}, t_{\mathrm{del}})$ hypercube is thus obtained by averaging $N = 3000$ normalized images [see Eqs. (3) and (4)] in 1 s. For each t_{del} delay, the t_{pu} and t_{pr} axes are scanned by acquiring 150 values corresponding to the birefringent wedge positions of both the ICPG and the ICS ranging from −0.8 to 1.2 mm, corresponding to t_{pu} and t_{pr} spanning from −55 to 82 fs. The typical acquisition

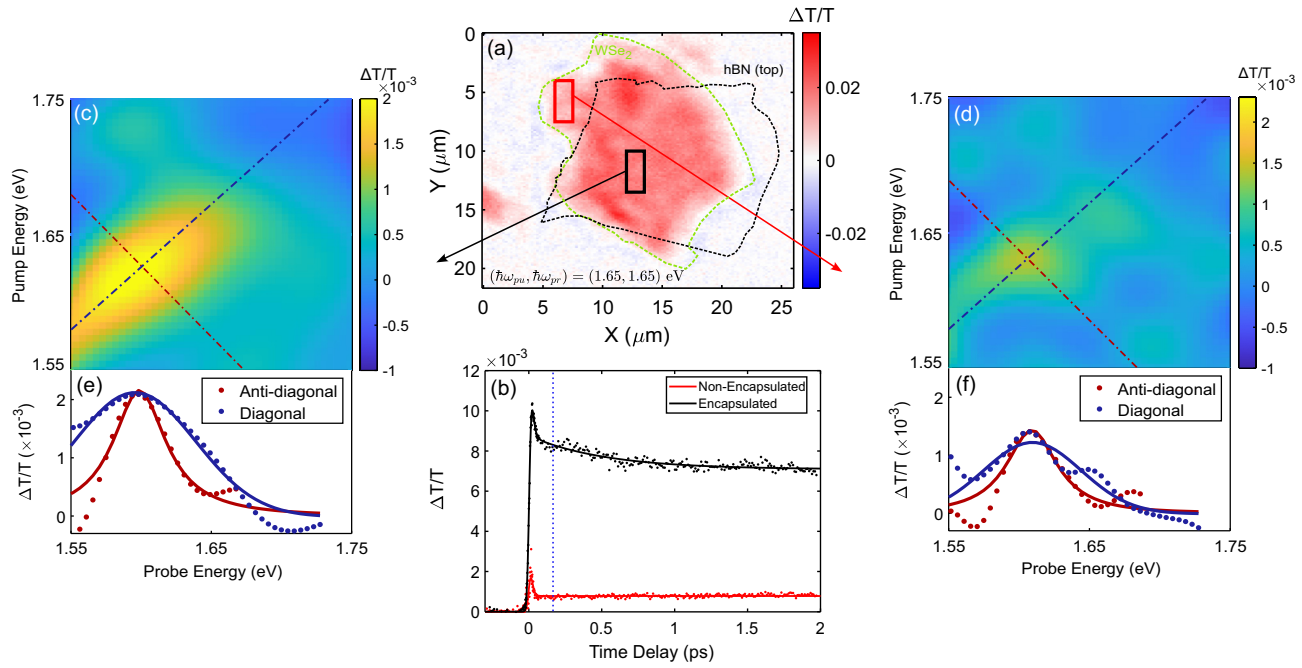


Fig. 6. 2DESM on bilayer WSe_2. (a) Spatially resolved signal. The $S(x, y; \omega_{pu}, \omega_{pr}, t_{del})$ signal acquired at $t_{del} = 150$ fs and for $\hbar\omega_{pu} = \hbar\omega_{pr} = 1.65$ eV is shown. The transmission variation has been normalized by taking the ratio between the measured signal and the total space and frequency dependent transmission. The black and red areas correspond to the fully encapsulated and unprotected bilayer WSe_2, as previously shown in Fig. 5(a). The contoured area in green highlights the WSe_2 region, while the black dashed contour marks the region encapsulated by hBN. (b) Time traces. Relaxation dynamics of the $S(x, y; t_{del})$ signal as a function of the pump–probe delay t_{del} obtained by integrating over the black and red areas and over the ω_{pu} and ω_{pr} frequency axes. The solid lines are the multi-exponential fits to the data. (c), (d) 2DES spectra. 2DES $S(x, y; \omega_{pu}, \omega_{pr}, t_{del})$ signals for fixed $t_{del} = 150$ fs and integrated over the black (c) and red (d) regions. The dashed blue lines represent the diagonal (ω) and the dashed red lines represent antidiagonal ($\tilde{\omega}$) directions, along which the lineshapes shown in panels (e), (f) have been extracted. (e), (f) Lineshape analysis. The panels report the diagonal (blue dots) and antidiagonal (red dots) lineshapes obtained by taking the line profiles of 2DES spectra [see panels (c), (d)] along the ω and $\tilde{\omega}$ directions. The blue and red curves represent the fits to Eqs. (9) and (10), respectively.

time for the full data cube shown in Fig. 2(a) is 10 h, depending on N and the number of steps in both the ICS and the ICPG. The frequency-domain signal is obtained via the FT [see Eq. (6)] of the time-domain data apodized using a symmetric sigmoid apodization window with a 0.5 mm width, chosen in order to maximize the SNR and reduce spectral artifacts.

Figure 6(a) shows the signal $S(x, y)$ extracted from the hypercube at the fixed pump and probe frequencies ($\hbar\omega_{pu} = \hbar\omega_{pr}$ 1.65 eV) and $t_{del} = 150$ fs. Under these resonant excitation conditions, the signal is expected to be dominated by the A-exciton of the bilayer WSe_2; however, since contributions from spectrally overlapping excitonic complexes such as trions cannot be excluded, we refrain from attributing the signal exclusively to the A-exciton. The green and black dashed lines indicate the WSe_2 bilayer and the hBN capping, respectively, as already shown in Fig. 5(a). Thanks to the capability of the technique to capture the spatial distribution of the transient transmissivity signal—measured simultaneously for all spatial locations within a single image—a spatial inhomogeneity of the signal across the sample is clearly visible. Here, we will focus on the difference between the fully capped region (black rectangular area) and the region that is not protected by the hBN overlayer (red rectangular area). The colorscale highlights a lower signal from the unprotected area, as compared to the one from the center of the sample that is fully encapsulated by hBN. This difference can be further shown in Fig. 6(b), where we plot the signal $S(t_{del})$ at the fixed pump and probe frequencies ($\hbar\omega_{pu} = \hbar\omega_{pr}$ 1.65 eV), integrated over the black and red regions, as a function of the pump–probe delay t_{del}. The signal from the fully encapsulated region is almost five times larger and presents a double exponential dynamics characterized by a fast decay on the order of the pulse width and a slower decay on the picosecond timescale. The signal from the unprotected region, in contrast, after a similar fast dynamics, reaches a quasi-stationary value, which corresponds to a plateau within the temporal window probed in the experiment. The temporal dynamics of the two regions have been reproduced by using the following time-dependent function:

$$f(t_{del}) = g(t_{del}) * \left[H(t_{del}) \cdot \left(\sum a_i e^{-t_{del}/\tau_i} + c \right) \right], \quad (8)$$

where $g(t_{del})$ is a Gaussian function accounting for the time resolution (see Section 2.C), $*$ represents the convolution, $H(t_{del})$ is a Heaviside function, a_i are the coefficients multiplying the exponential decays with time constants τ_i, and c is a constant accounting for the steady-state value at $t_{del} = 2$ ps. The best fitting for the fully protected region is obtained by using $\tau_1 = 12 \pm 4$ fs and $\tau_2 = 0.5 \pm 0.1$ ps, whereas for the unprotected region, the best fitting is obtained by using a single exponential decay with $\tau_1 = 8 \pm 5$ fs.

Additional insights on the exciton dynamics are given by the analysis of the 2DES maps shown in Fig. 6. Figs. 6(c) and 6(d) show $S(\omega_{pu}, \omega_{pr})$ for the fixed time delay $t_{del} = 150$ fs and integrated over the black Fig. 6(c) and red Fig. 6(d)] areas. In the fully encapsulated area, the signal is centered at 1.598 ± 0.002 eV (extracted from the diagonal line profile discussed below) and has an elliptical

shape with a pronounced elongation along the diagonal axis, which is typical of systems in which disorder-driven inhomogeneous broadening is larger than the inverse of the intrinsic lifetime. Fig. 6(e) shows the lineshapes along the diagonal (ω) and antidiagonal ($\tilde{\omega}$) axes. Considering that in the partially collinear geometry [56], the 2DES signal measures the purely absorptive spectrum, which corresponds to the sum of the real part of rephasing and non-rephasing signals, the diagonal lineshape is described by the function [69,70]

$$S_{\mathrm{diag}}(\omega) = A\left[\Re\left\{\frac{1}{\sigma(\gamma - i(\omega-\omega_0))}\exp\left(\frac{(\gamma - i(\omega-\omega_0))^2}{2\sigma^2}\right)\times\left[1-\mathrm{erf}\left(\frac{\gamma - i(\omega-\omega_0)}{\sqrt{2}\,\sigma}\right)\right]\right\}\right] \tag{9}$$

and the antidiagonal lineshape by [69,70]

$$S_{\mathrm{antidiag}}(\tilde{\omega}) = A\left[\frac{1}{\gamma^2 + (\tilde{\omega}-\omega_0)^2} * \exp\left(-\frac{(\tilde{\omega}-\omega_0)^2}{2\sigma^2}\right)\right], \tag{10}$$

where A is an amplitude coefficient, ω_0 is the central excitonic frequency, σ is the disorder-induced inhomogeneous broadening, and γ is the intrinsic linewidth, whose inverse represents the actual lifetime of the exciton. The global fitting procedure applied to the diagonal and antidiagonal lineshapes returns $\gamma = 23 \pm 2$ meV and $\sigma = 40 \pm 1$ meV for the fully encapsulated WSe_2 bilayer. The inhomogeneous broadening is larger than the intrinsic linewidth, suggesting an important role played by the local disorder. The inverse intrinsic linewidth, i.e., $\hbar/\gamma \simeq 29 \pm 2$ fs, represents the actual decoherence time of the system, driven by the fastest scattering processes that can take place in the material. This short decoherence time is smaller than the values reported in the literature for monolayer TMDs at low temperature [49,51,71,72], as a consequence of the increased temperature-induced scattering with optical phonons [47,48] and the additional linewidth broadening ubiquitously observed in the bilayer, compared to monolayer samples [73]. These data suggest the rapid formation of an incoherent excitonic gas, which relaxes on the timescale $t_2 = 0.5 \pm 0.1$ ps [see Fig. 6(b)] due to the decay of $K-K$ direct excitons into $K-Q$ momentum-forbidden dark excitons [74,75], as observed by the recent momentum-resolved photoemission experiment [76].

In the unprotected region [red area in Fig. 6(a)], we observe a suppression of the 2DES signal amplitude, which is centered at 1.611 ± 0.003 eV. The 13 ± 5 meV energy shift compared to the fully encapsulated region [black area in Fig. 6(a)] is due to the different screening effects that influence the exciton photon energy, as already reported in the literature [72,77–79]. Lineshape analysis [Fig. 6(f)] similar to what has been done for the encapsulated region returns an intrinsic linewidth $\gamma = 22 \pm 3$ meV, corresponding to $\hbar/\gamma \simeq 30 \pm 4$ fs decoherence time. The comparable intrinsic linewidth in the encapsulated and non-encapsulated regions suggests that, at room temperature, dephasing processes are dominated by scattering with thermally activated phonons [47,48,72], which are not affected by the hBN overlayer.

4. TEMPERATURE-DEPENDENT 2DESM

To benchmark the 2DESM setup under cryogenic operating conditions, temperature-dependent measurements were performed on an hBN-encapsulated bulk WSe_2 flake. Figure 7(a) shows an optical microscopy image of the employed sample, highlighted by the yellow contour. 2DESM measurements were carried out at $T = 300$ K and $T = 20$ K, for a fixed pump–probe delay $t_{\mathrm{del}} = 50$ fs, under the same experimental conditions of the data presented in Section 3, including the excitation fluence, beam spot size, and image acquisition rate. At both temperatures, t_{pu} and t_{pr} axes were scanned over the range $[-55, 120]$ fs, yielding a spectral resolution improved by ≈ 1.5-fold, as compared to data presented in Section 3.

The 2DESM maps extracted from the central region of the flake [blue contour in Fig. 7(a)] are shown in Figs. 7(b) and 7(c) for $T = 300$ K and $T = 20$ K, respectively. The low-temperature spectrum exhibits a fivefold enhancement of the excitonic resonance intensity, consistent with the reduction of exciton–phonon scattering [80]. Concurrently, a blueshift by 90 meV is observed in the excitonic resonance energy, which moves from 1.600 ± 0.005 eV at $T = 300$ K to 1.693 ± 0.003 eV at $T = 20$ K, as highlighted by the horizontal line cuts displayed above each 2DES map, obtained by averaging the signal within the gray horizontal lines. This temperature-induced blueshift is in good agreement with previously reported values for bulk WSe_2 [80] and is attributed to bandgap renormalization driven by the progressive freezing of electron–phonon interactions and the consequent quenching of phonon-assisted sub-bandgap transitions upon cooling [80–82].

Beyond the spectral shift, temperature-dependent measurements reveal a pronounced evolution of the excitonic lineshape, reflecting substantial modifications of the exciton–phonon coupling strength and, consequently, of the intrinsic exciton decoherence time. The antidiagonal line cuts extracted at both temperatures are shown in Fig. 7(d), where a clear temperature-driven narrowing of the antidiagonal linewidth is evident. Fitting Eq. (10) to the experimental data yields a homogeneous linewidth that decreases from $\gamma = 25 \pm 6$ meV at room temperature to $\gamma = 17 \pm 5$ meV at 20 K, consistent with the low-temperature suppression of exciton–phonon scattering channels. This linewidth narrowing corresponds to an increase in the exciton decoherence time from $\tau = \hbar/\gamma \simeq 26 \pm 6$ fs at room temperature to $\tau = \hbar/\gamma \simeq 40 \pm 10$ fs at 20 K. These observations demonstrate that, at high temperature, the exciton decoherence is accelerated by the coupling to the phonon thermal bath. Consistent with previous spatially integrated 2DES studies [83] and coherent spectroscopy investigations in transition metal dichalcogenides [36], the excitonic coherence is enhanced at low temperature due to reduced dephasing and approaches a low-temperature limit set by radiative recombination and disorder in the material. Overall, these findings demonstrate the capability of 2DESM to investigate excitonic coherence and dephasing processes as a function of temperature in quantum materials.

5. CONCLUSION

In conclusion, we have developed a widefield two-dimensional electronic spectroscopy microscope (2DESM) that unifies multidimensional spectroscopy with optical imaging, enabling simultaneous femtosecond temporal, micrometer spatial, and broadband spectral resolution. This approach overcomes intrinsic limitations of pump–probe spectro-microscopy, which lacks sensitivity to quantum-coherent polarization dynamics and provides only population-based information. Compared to existing point-scanning 2DES microscopy approaches that require tight

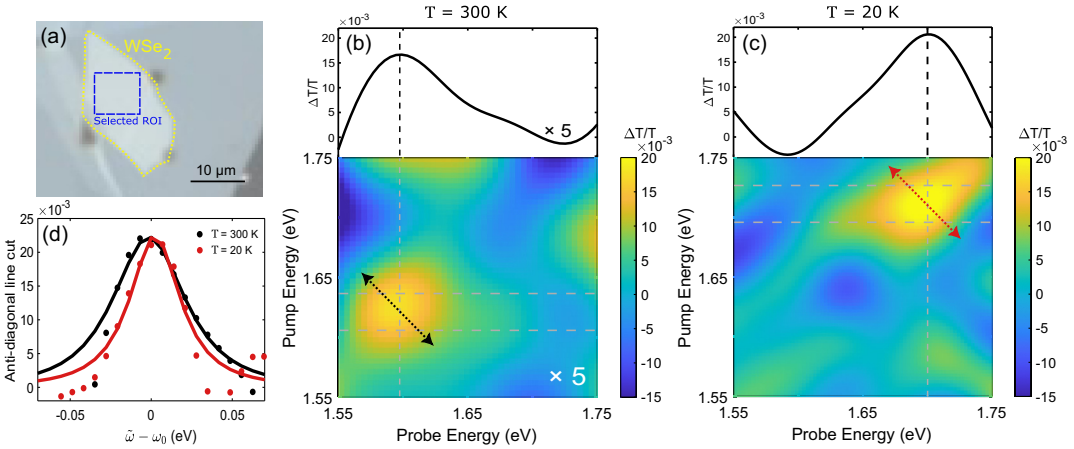


Fig. 7. 2DESM measurements on bulk WSe_2. (a) Optical microscopy image of the hBN-encapsulated sample. The yellow contour outlines the bulk WSe_2 region, while the blue rectangle indicates the area used for spatially averaging and extraction of the 2D maps. (b) 2DES map acquired at T = 300 K and $t_{del} = 50$ fs. The upper panel shows the pump-integrated signal obtained by integrating the 2D map over the pump-energy range defined by the horizontal gray dashed line, revealing the excitonic resonance centered at 1.6 eV. For clarity, the signal amplitude is multiplied by a factor of five. (c) 2DES map acquired at T = 20 K and $t_{del} = 50$ fs. The upper panel shows the pump-integrated signal obtained by integrating the 2D map over the pump-energy range defined by the horizontal gray dashed line, with the excitonic resonance centered at 1.7 eV.(d) Antidiagonal line cuts at $t_{del} = 50$ fs for both temperatures, together with fits along the $\tilde{\omega}$ direction. Solid lines correspond to fits using Eq. (10).

focusing with transmission objectives, 2DESM offers the key advantages of parallel spatial acquisition across the full field of view, enabling high-throughput hyperspectral imaging without the need for sequential raster scanning. Moreover, because no objective is employed in the excitation path, the technique supports a broader spectral bandwidth and higher temporal resolution. This comes at the cost of a moderate reduction in spatial resolution (~ 1 μm) relative to diffraction-limited confocal implementations ($\sim 0.3-0.5$ μm) [47–51]. As a proof of concept, we applied 2DESM to the bilayer WSe_2 encapsulated in hBN and resolved spatial variations in the A-exciton response. Encapsulated regions exhibited stronger 2DES signals, pronounced inhomogeneous broadening, and fast exciton decoherence ($\gamma = 23 \pm 2$ meV), followed by a 0.5 ps relaxation into momentum-dark excitonic states. In contrast, uncapped regions showed a reduced amplitude and a different relaxation pathway. Temperature-dependent measurements reveal a clear excitonic blueshift and enhanced coherence, associated with the low-temperature quenching of phonon fluctuations. These results demonstrate the possibility of directly correlating the local structural environment with quantum-coherent exciton dynamics, validating 2DESM as a general platform for interrogating disorder, dephasing, and energy-transfer processes in heterogeneous quantum-confined systems and for directly investigating these phenomena under cryogenic operating conditions.

2DESM, therefore, opens new opportunities for studying ultrafast quantum phenomena in real space, addressing open questions in excitonics and correlated material optoelectronics [52] that remain challenging to investigate using pump–probe imaging or scanning-based 2DES. 2DESM has the capability to: (i) resolve the intrinsic coherence limits at the microscale in van der Waals heterostructures, including systems with interlayer excitons and moiré-trapped states; (ii) map the microscale landscape of disorder, allowing quantitative comparison of intrinsic linewidths versus inhomogeneous broadening across device architectures; (iii) study many-body interactions and emergent quasiparticles, such as biexcitons and trions, tracking where they form and how they propagate microscopically; and (iv) probe non-local coupling [50] and energy transport, including coherent exciton diffusion and cavity-enhanced delocalization in photonic–TMD or semiconductor hybrids.

By unifying optical microscopy, quantum-coherence spectroscopy, and high-throughput hyperspectral imaging, 2DESM establishes a powerful experimental direction for quantum materials research, providing a novel perspective on the interplay between the local structure, disorder, dielectric environment, and ultrafast electronic coherence in emerging nanoscale technologies.

Funding. Ministero dell'università e della ricerca (PRIN 2020JLZ52N-003).

Acknowledgment. M. Azarm, R. Asif, A. Milloch, Fr. Proietto, F. Bianco, and C. Giannetti acknowledge financial support from MIUR through the PRIN 2020 (Prot. 2020JLZ52N-003). The authors also thank S. Pezzini for insightful discussions.

Disclosures. The authors declare no conflicts of interest.

Data availability. Data underlying the results presented in this paper are not publicly available at this time but may be obtained from the authors upon reasonable request.

REFERENCES

1. S. Biswas, J. Kim, X. Zhang, *et al.*, "Coherent two-dimensional and broadband electronic spectroscopies," Chem. Rev. **122**, 4257–4321 (2022).
2. Z. Wang, M. Wang, T. Heine, *et al.*, "Electronic and quantum properties of organic two-dimensional crystals," Nat. Rev. Mater. **10**, 147–166 (2025).
3. Y. Liu, N. O. Weiss, X. Duan, *et al.*, "Van der Waals heterostructures and devices," Nat. Rev. Mater. **1**, 16042 (2016).
4. J. Li, X. Yang, Y. Liu, *et al.*, "General synthesis of two-dimensional van der Waals heterostructure arrays," Nature **579**, 368–374 (2020).
5. J.-S. Lee, M. V. Kovalenko, J. Huang, *et al.*, "Band-like transport, high electron mobility and high photoconductivity in all-inorganic nanocrystal arrays," Nat. Nanotechnol. **6**, 348–352 (2011).
6. L. Protesescu, S. Yakunin, M. I. Bodnarchuk, *et al.*, "Nanocrystals of cesium lead halide perovskites ($CsPbX_3$, X = Cl, Br, and I): novel optoelectronic materials showing bright emission with wide color gamut," Nano Lett. **15**, 3692–3696 (2015).

7. G. Rainò, M. A. Becker, M. I. Bodnarchuk, *et al.*, "Superfluorescence from lead halide perovskite quantum dot superlattices," Nature **563**, 671–675 (2018).
8. A. Milloch, U. Filippi, P. Franceschini, *et al.*, "Halide perovskite artificial solids as a new platform to simulate collective phenomena in doped Mott insulators," Nano Lett. **23**, 10617–10624 (2023).
9. S. Liu, X. Li, H. Liu, *et al.*, "Super-resolved snapshot hyperspectral imaging of solid-state quantum emitters for high-throughput integrated quantum technologies," Nat. Photonics **18**, 967–974 (2024).
10. S. Manzeli, D. Ovchinnikov, D. Pasquier, *et al.*, "2D transition metal dichalcogenides," Nat. Rev. Mater. **2**, 17033 (2017).
11. G. Wang, A. Chernikov, M. M. Glazov, *et al.*, "Colloquium: Excitons in atomically thin transition metal dichalcogenides," Rev. Mod. Phys. **90**, 021001 (2018).
12. P. Rivera, H. Yu, K. L. Seyler, *et al.*, "Interlayer valley excitons in heterobilayers of transition metal dichalcogenides," Nat. Nanotechnol. **13**, 1004–1015 (2018).
13. C. Jin, E. C. Regan, A. Yan, *et al.*, "Observation of moiré excitons in WSe_2/WS_2 heterostructure superlattices," Nature **567**, 76–80 (2019).
14. K. Tran, G. Moody, F. Wu, *et al.*, "Evidence for moiré excitons in van der Waals heterostructures," Nature **567**, 71–75 (2019).
15. M. H. Naik, E. C. Regan, Z. Zhang, *et al.*, "Intralayer charge-transfer moiré excitons in van der Waals superlattices," Nature **609**, 52–57 (2022).
16. L. Du, "New excitons in multilayer 2D materials," Nat. Rev. Phys. **6**, 157–159 (2024).
17. K. L. Seyler, P. Rivera, H. Yu, *et al.*, "Signatures of moiré-trapped valley excitons in $MoSe_2/WSe_2$ heterobilayers," Nature **567**, 66–70 (2019).
18. Z. Zhang, Y. Wang, K. Watanabe, *et al.*, "Flat bands in twisted bilayer transition metal dichalcogenides," Nat. Phys. **16**, 1093–1096 (2020).
19. J. Choi, W.-T. Hsu, L.-S. Lu, *et al.*, "Moiré potential impedes interlayer exciton diffusion in van der Waals heterostructures," Sci. Adv. **6**, eaba8866 (2020).
20. A. Chernikov, C. Ruppert, H. M. Hill, *et al.*, "Population inversion and giant bandgap renormalization in atomically thin WS_2 layers," Nat. Photonics **9**, 466–470 (2015).
21. D. Guerci, M. Capone, and M. Fabrizio, "Exciton Mott transition revisited," Phys. Rev. Mater. **3**, 054605 (2019).
22. G. Wang, L. Bouet, D. Lagarde, *et al.*, "Valley dynamics probed through charged and neutral exciton emission in monolayer WSe_2," Phys. Rev. B **90**, 075413 (2014).
23. L. E. P. López, A. Rosławska, F. Scheurer, *et al.*, "Tip-induced excitonic luminescence nanoscopy of an atomically resolved van der Waals heterostructure," Nat. Mater. **22**, 482–488 (2023).
24. R. Krause, S. Aeschlimann, M. Chávez-Cervantes, *et al.*, "Microscopic understanding of ultrafast charge transfer in van der Waals heterostructures," Phys. Rev. Lett. **127**, 276401 (2021).
25. F. Fabbri, S. Raha, and F. Bianco, "The interplay between neutral and charged excitons driven by electron irradiation in monolayer WSe_2," Mater. Sci. Semicond. Process. **191**, 109373 (2025).
26. X. Sui, H. Wang, C. Liang, *et al.*, "Ultrafast internal exciton dissociation through edge states in MoS_2 nanosheets with diffusion blocking," Nano Lett. **22**, 5651–5658 (2022).
27. M. Domke, S. Rapp, M. Schmidt, *et al.*, "Ultrafast pump-probe microscopy with high temporal dynamic range," Opt. Express **20**, 10330–10338 (2012).
28. C. Schnedermann, J. M. Lim, T. Wende, *et al.*, "Sub-10 fs time-resolved vibronic optical microscopy," J. Phys. Chem. Lett. **7**, 4854–4859 (2016).
29. G. Piland and E. M. Grumstrup, "High-repetition rate broadband pump–probe microscopy," J. Phys. Chem. A **123**, 8709–8716 (2019).
30. Z. Chen, G. Dong, and J. Qiu, "Ultrafast pump-probe spectroscopy—a powerful tool for tracking spin-quantum dynamics in metal halide perovskites," Adv. Quantum Technol. **4**, 2100052 (2021).
31. Q. Cui, F. Ceballos, N. Kumar, *et al.*, "Transient absorption microscopy of monolayer and bulk WSe_2," ACS Nano **8**, 2970–2976 (2014).
32. Z. Zhang, J. Sung, D. T. W. Toolan, *et al.*, "Ultrafast exciton transport at early times in quantum dot solids," Nat. Mater. **21**, 533–539 (2022).
33. A. Genco, C. Trovatello, C. Louca, *et al.*, "Ultrafast exciton and trion dynamics in high-quality encapsulated MoS_2 monolayers," Phys. Status Solidi (B) **260**, 2200376 (2023).
34. F. Faini, Y. Asensio, F. Visentin, *et al.*, "Imaging ultrafast charge transfer at low-dimensional lead halide perovskite heterostructures," ACS Energy Lett. **10**, 120–127 (2025).
35. C. Trovatello, F. Katsch, N. J. Borys, *et al.*, "The ultrafast onset of exciton formation in 2D semiconductors," Nat. Commun. **11**, 5277 (2020).
36. G. Moody, C. K. Dass, K. Hao, *et al.*, "Intrinsic homogeneous linewidth and broadening mechanisms of excitons in monolayer transition metal dichalcogenides," Nat. Commun. **6**, 8315 (2015).
37. T. L. Purz, E. W. Martin, P. Rivera, *et al.*, "Coherent exciton-exciton interactions and exciton dynamics in a $MoSe_2/WSe_2$ heterostructure," Phys. Rev. B **104**, L241302 (2021).
38. S. T. Cundiff and S. Mukamel, "Optical multidimensional coherent spectroscopy," Phys. Today **66**, 44–49 (2013).
39. C. L. Smallwood and S. T. Cundiff, "Multidimensional coherent spectroscopy of semiconductors," Laser Photonics Rev. **12**, 1800171 (2018).
40. J. Kim, S. Mukamel, and G. D. Scholes, "Two-dimensional electronic double-quantum coherence spectroscopy," Acc. Chem. Res. **42**, 1375–1384 (2009).
41. E. Collini, "2D electronic spectroscopic techniques for quantum technology applications," J. Phys. Chem. C **125**, 13096–13108 (2021).
42. K. J. Czech, B. J. Thompson, S. Kain, *et al.*, "Measurement of ultrafast excitonic dynamics of few-layer MoS_2 using state-selective coherent multidimensional spectroscopy," ACS Nano **9**, 12146–12157 (2015).
43. M. Maiuri, M. Garavelli, and G. Cerullo, "Ultrafast spectroscopy: state of the art and open challenges," J. Am. Chem. Soc. **142**, 3–15 (2019).
44. D. Timmer, M. Gittinger, T. Quenzel, *et al.*, "Ultrafast coherent exciton couplings and many-body interactions in monolayer WS_2," Nano Lett. **24**, 8117–8125 (2024).
45. G. Bressan, D. Green, G. A. Jones, *et al.*, "Two-dimensional electronic spectroscopy resolves relative excited-state displacements," J. Phys. Chem. Lett. **15**, 2876–2884 (2024).
46. I. Kuznetsova, T. Meier, S. T. Cundiff, *et al.*, "Determination of homogeneous and inhomogeneous broadening in semiconductor nanostructures by two-dimensional Fourier-transform optical spectroscopy," Phys. Rev. B **76**, 153301 (2007).
47. T. Jakubczyk, V. Delmonte, M. Koperski, *et al.*, "Radiatively limited dephasing and exciton dynamics in $MoSe_2$ monolayers revealed with four-wave mixing microscopy," Nano Lett. **16**, 5333–5339 (2016).
48. T. Jakubczyk, K. Nogajewski, M. R. Molas, *et al.*, "Impact of environment on dynamics of exciton complexes in a WS_2 monolayer," 2D Mater. **5**, 031007 (2018).
49. T. Jakubczyk, G. Nayak, L. Scarpelli, *et al.*, "Coherence and density dynamics of excitons in a single-layer MoS_2 reaching the homogeneous limit," ACS Nano **13**, 3500–3511 (2019).
50. A. Liu, E. W. Martin, J. Hu, *et al.*, "Nonlocal coherent optical nonlinearities of a macroscopic quantum system," Phys. Rev. Lett. **135**, 183801 (2025).
51. W. Luo, B. G. Whetten, V. Kravtsov, *et al.*, "Ultrafast nanoimaging of electronic coherence of monolayer WSe_2," Nano Lett. **23**, 1767–1773 (2023).
52. E. C. Regan, D. Wang, E. Y. Paik, *et al.*, "Emerging exciton physics in transition metal dichalcogenide heterobilayers," Nat. Rev. Mater. **7**, 778–795 (2022).
53. S. Mukamel, *Principles of Nonlinear Optical Spectroscopy* (Oxford University Press, 1995).
54. D. M. Jonas, "Two-dimensional femtosecond spectroscopy," Annu. Rev. Phys. Chem. **54**, 425–463 (2003).
55. P. Hamm and M. Zanni, *Concepts and Methods of 2D Infrared Spectroscopy* (Cambridge University Press, 2011).
56. F. D. Fuller and J. P. Ogilvie, "Experimental implementations of two-dimensional Fourier transform electronic spectroscopy," Annu. Rev. Phys. Chem. **66**, 667–690 (2015).
57. C. Giannetti, "New perspectives in the ultrafast spectroscopy of many-body excitations in correlated materials," Il Nuovo Cimento C **39**, 279 (2016).
58. D. Brida, C. Manzoni, and G. Cerullo, "Phase-locked pulses for two-dimensional spectroscopy by a birefringent delay line," Opt. Lett. **37**, 3027–3029 (2012).
59. M. Hörmann, F. Visentin, S. K. Chakraborty, *et al.*, "Self-referencing for quasi shot-noise-limited widefield transient microscopy," Opt. Express **32**, 21230–21242 (2024).
60. R. Wu, Y. Zhang, M. Shahjahan, *et al.*, "Self-referencing ultrafast widefield pump-probe microscopy," Nat. Commun. **16**, 9686 (2025).
61. A. Candeo, B. E. Nogueira de Faria, M. Erreni, *et al.*, "A hyperspectral microscope based on an ultrastable common-path interferometer," APL Photonics **4**, 120802 (2019).

62. R. Trebino, K. W. DeLong, D. N. Fittinghoff, *et al.*, "Measuring ultrashort laser pulses in the time-frequency domain using frequency-resolved optical gating," Rev. Sci. Instrum. **68**, 3277–3295 (1997).
63. A. Perri, B. E. Nogueira de Faria, D. C. T. Ferreira, *et al.*, "Hyperspectral imaging with a TWINS birefringent interferometer," Opt. Express **27**, 15956–15967 (2019).
64. D. Eimerl, L. Davis, S. Velsko, *et al.*, "Optical, mechanical, and thermal properties of barium borate," J. Appl. Phys. **62**, 1968–1983 (1987).
65. A. Hanbicki, M. Currie, G. Kioseoglou, *et al.*, "Measurement of high exciton binding energy in the monolayer transition-metal dichalcogenides WS_2 and WSe_2," Solid State Commun. **203**, 16–20 (2015).
66. K. P. O'Donnell and X. Chen, "Temperature dependence of semiconductor band gaps," Appl. Phys. Lett. **58**, 2924–2926 (1991).
67. W. Zhao, Z. Ghorannevis, L. Chu, *et al.*, "Evolution of electronic structure in atomically thin sheets of WS_2 and WSe_2," ACS Nano **7**, 791–797 (2013).
68. P. Tonndorf, R. Schmidt, P. Böttger, *et al.*, "Photoluminescence emission and Raman response of monolayer MoS_2, $MoSe_2$, and WSe_2," Opt. Express **21**, 4908–4916 (2013).
69. M. E. Siemens, G. Moody, H. Li, *et al.*, "Resonance lineshapes in two-dimensional Fourier transform spectroscopy," Opt. Express **18**, 17699–17708 (2010).
70. A. Milloch, U. Filippi, P. Franceschini, *et al.*, "Fate of optical excitons in $FAPbI_3$ nanocube superlattices," ACS Photonics **11**, 3511–3520 (2024).
71. P. Dey, J. Paul, Z. Wang, *et al.*, "Optical coherence in atomic-monolayer transition-metal dichalcogenides limited by electron-phonon interactions," Phys. Rev. Lett. **116**, 127402 (2016).
72. F. Cadiz, E. Courtade, C. Robert, *et al.*, "Excitonic linewidth approaching the homogeneous limit in MoS_2-based van der Waals heterostructures," Phys. Rev. X **7**, 021026 (2017).
73. A. Raja, M. Selig, G. Berghauser, *et al.*, "Enhancement of exciton–phonon scattering from monolayer to bilayer WSe_2," Nano Lett. **18**, 6135–6143 (2018).
74. J. Shi, V. Turkowski, and T. S. Rahman, "Dark-exciton energy splitting in monolayer WSe_2: insights from time-dependent density functional theory," Phys. Rev. B **107**, 155431 (2023).
75. J. Lindlau, M. Selig, A. Neumann, *et al.*, "The role of momentum-dark excitons in the elementary optical response of bilayer WSe_2," Nat. Commun. **9**, 2586 (2018).
76. J. Madéo, M. K. L. Man, C. Sahoo, *et al.*, "Directly visualizing the momentum-forbidden dark excitons and their dynamics in atomically thin semiconductors," Science **370**, 1199–1204 (2020).
77. S. Borghardt, J.-S. Tu, F. Winkler, *et al.*, "Engineering of optical and electronic band gaps in transition metal dichalcogenide monolayers through external dielectric screening," Phys. Rev. Mater. **1**, 054001 (2017).
78. I. C. Gerber and X. Marie, "Dependence of band structure and exciton properties of encapsulated WSe_2 monolayers on the hBN-layer thickness," Phys. Rev. B **98**, 245126 (2018).
79. H. C. Nerl, J. P. Guerrero-Felipe, A. M. Valencia, *et al.*, "Mapping the energy-momentum dispersion of hBN excitons and hybrid plasmons in hBN-WSe_2 heterostructures," npj 2D Mater. Appl. **8**, 68 (2024).
80. A. Arora, M. Koperski, K. Nogajewski, *et al.*, "Excitonic resonances in thin films of WSe_2: from monolayer to bulk material," Nanoscale **7**, 10421–10429 (2015).
81. H. Mishra, A. Bose, A. Dhar, *et al.*, "Exciton-phonon coupling and band-gap renormalization in monolayer WSe_2," Phys. Rev. B **98**, 045143 (2018).
82. W. Ali, Y. Liu, M. Huang, *et al.*, "Temperature-dependent phonon scattering and photoluminescence in vertical MoS_2/WSe_2 heterostructures," Nanomaterials **13**, 2349 (2023).
83. K. Hao, G. Moody, F. Wu, *et al.*, "Direct measurement of exciton valley coherence in monolayer WSe_2," Nat. Phys. **12**, 677–682 (2016).